THE JOURNAL OF CHEMICAL PHYSICS **134**, 054301 (2011)

Chloroacetone photodissociation at 193 nm and the subsequent dynamics of the $CH_3C(O)CH_2$ radical—an intermediate formed in the OH + allene reaction *en route* to CH_3 + ketene

Bridget W. Alligood,[1] Benjamin L. FitzPatrick,[1] David E. Szpunar,[2,a)] and Laurie J. Butler[1,a)]
[1]*The James Franck Institute and Department of Chemistry, University of Chicago, Chicago, Illinois 60637, USA*
[2]*Department of Biological, Chemical, and Physical Sciences, Roosevelt University, Schaumburg, Illinois 60173, USA*

(Received 4 August 2010; accepted 18 November 2010; published online 1 February 2011)

We use a combination of crossed laser-molecular beam experiments and velocity map imaging experiments to investigate the primary photofission channels of chloroacetone at 193 nm; we also probe the dissociation dynamics of the nascent $CH_3C(O)CH_2$ radicals formed from C–Cl bond fission. In addition to the C–Cl bond fission primary photodissociation channel, the data evidence another photodissociation channel of the precursor, C–C bond fission to produce CH_3CO and CH_2Cl. The $CH_3C(O)CH_2$ radical formed from C–Cl bond fission is one of the intermediates in the OH + allene reaction *en route* to CH_3 + ketene. The 193 nm photodissociation laser allows us to produce these $CH_3C(O)CH_2$ radicals with enough internal energy to span the dissociation barrier leading to the CH_3 + ketene asymptote. Therefore, some of the vibrationally excited $CH_3C(O)CH_2$ radicals undergo subsequent dissociation to CH_3 + ketene products; we are able to measure the velocities of these products using both the imaging and scattering apparatuses. The results rule out the presence of a significant contribution from a C–C bond photofission channel that produces CH_3 and $COCH_2Cl$ fragments. The $CH_3C(O)CH_2$ radicals are formed with a considerable amount of energy partitioned into rotation; we use an impulsive model to explicitly characterize the internal energy distribution. The data are better fit by using the C–Cl bond fission transition state on the S_1 surface of chloroacetone as the geometry at which the impulsive force acts, not the Franck–Condon geometry. Our data suggest that, even under atmospheric conditions, the reaction of OH with allene could produce a small branching to CH_3 + ketene products, rather than solely producing inelastically stabilized adducts. This additional channel offers a different pathway for the OH-initiated oxidation of such unsaturated volatile organic compounds, those containing a C=C=C moiety, than is currently included in atmospheric models. © *2011 American Institute of Physics*. [doi:10.1063/1.3525465]

I. INTRODUCTION

While the photodissociation of chloroacetone is of some atmospheric interest in and of itself, the $CH_3C(O)CH_2$ product formed from C–Cl bond fission is also an intermediate in the OH + allene reaction.[1] The OH-initiated oxidation of volatile organic compounds (VOCs) is of central importance in atmospheric chemistry, particularly in the formation of secondary organic aerosols (SOAs). Allene contains the same C=C=C functional group as 1,2-butadiene and 3-methyl-1,2-butadiene, so the OH + allene reaction may elucidate the reactions of OH with these volatile fuel constituents. Predicting the branching for these types of bimolecular reactions relies heavily on energetically accurate dissociation and isomerization pathways of the radical intermediates involved. As such, experimental validation of calculated barrier heights helps develop these predictive tools and could be used to benchmark emerging electronic structure methods.

Burkholder *et al.* measured the ultraviolet (UV) absorption cross sections and photodissociation quantum yields of chloroacetone.[2] These studies involved a bulk kinetic system, so they were not able to resolve the primary photodissociation channels. Previous photodissociation experiments, both at 248 and 308 nm, show that chloroacetone exhibits two primary photofission channels: C–C bond fission and C–Cl bond fission.[3,4] Neither of these experiments had photon energies that allowed for the radicals to be formed with enough internal energy to surmount the subsequent dissociation barrier to CH_3 + ketene, which lies 39.5 kcal/mol above the zero-point energy of the $CH_3C(O)CH_2$ radical.

Raman *et al.*[1] commented on the potential differences in the reaction of OH with allene when the OH adds to the central C atom. The resonance-stabilized radical that is formed in the addition of the OH radical to the center C atom has a lower energy barrier to isomerization, and ultimately to dissociation to CH_3 + ketene, than proceeding back out to the OH + allene asymptote. This could have important ramifications with respect to the kinetic mechanisms involved in the

---

[a)] Authors to whom correspondence should be addressed. Electronic addresses: L-Butler@uchicago.edu and dszpunar@roosevelt.edu.

0021-9606/2011/134(5)/054301/13/$30.00

chemistry of these volatile organic compounds; we refer to this in the Discussion.

II. METHODS

Two complementary experimental techniques are described in the following sections. The majority of the data was taken with the crossed laser-molecular beam scattering apparatus, described first, and supplementary imaging experiments were performed to help analyze some of the more complicated electron impact spectra.

A. Experimental method—Scattering apparatus

We use a crossed laser-molecular beam scattering apparatus to measure the photofragment velocities resulting from the photodissociation of chloroacetone, $CH_3C(O)CH_2Cl$, as well as any products from the unimolecular dissociation of nascent $CH_3C(O)CH_2$ radicals formed during the initial C–Cl bond fission. We expand the molecular beam, composed of the equilibrium vapor pressure of $CH_3C(O)CH_2Cl$ at 15 °C and seeded in He to a total pressure of 400 Torr, through a continuous (not pulsed) nozzle. We heat the nozzle, having an orifice diameter of approximately 0.15 mm, to 180 °C. The beam passes through two skimmers before it enters the main chamber. There, it intersects the output of a pulsed 193.3 nm laser, with light produced by the ArF transition of an unpolarized Lumonics PM-848 excimer laser. We focus the laser pulses down to a beam spot with a $\sim 6\ \mathrm{mm}^2$ cross-sectional area in the interaction region. Over the course of the experiment, we maintained a laser power of roughly 15 mJ/pulse.

The laser light propagates along an axis that is perpendicular to the plane defined by the molecular beam and the detector axis, resulting in light that is unpolarized in the scattering plane. The nozzle is contained within the source region, which we rotate in order to facilitate data collection at different source angles. The neutral photodissociation products scatter from the interaction region with velocities determined by the vector sum of the molecular beam velocity and the recoil velocity imparted during the photodissociation. Those scattering into the 1.5° acceptance angle of the differentially pumped detector travel 45.0 cm to an electron bombardment ionizer, where they are ionized by 200 eV electrons.[5] High voltage lenses accelerate and focus these ions toward the entrance of a quadrupole mass spectrometer, where they are mass-selected and detected using a Daly detector.[6] The resultant voltage pulses are counted by a multichannel scaler; the resulting signal is proportional to the number of ions at each mass-to-charge ratio, detected as a function of time after the dissociating light pulse. We accumulate the signal in 2 μs channels, and we plot all data and fit points at the end of each time window. The signal has contributions from parent and daughter ions of the neutral photofragments, as well as the products formed from the secondary dissociation of any unstable radicals. Upon subtraction of the calibrated ion flight time, calculated using the apparatus' measured ion flight constant of 4.5 $\mu\mathrm{s\ amu}^{-1/2}$, forward convolution fitting of the time-of-flight (TOF) spectrum determines the distribution of energies imparted to relative product translation during the dissociation, E_T.

To characterize the parent beam, we align the source along the detector axis and raise a 300 Hz chopper wheel into the beam. To calibrate the neutral flight path, we use a He beam and an unheated nozzle. The number density distribution of velocities in the molecular beam typically peaks at 1600 m/s, with a FWHM of 11%. To measure the velocities of the neutral photofragments reported in this paper, the molecular beam source is rotated to different angles in the plane containing the beam and detector axis, which is perpendicular to the laser beam propagation direction. The angle at which data are acquired is indicated in the upper right corner of all presented spectra.

Chloroacetone, upon photodissociation at 193 nm, yields the $CH_3C(O)CH_2$ radical, an intermediate *en route* to CH_3 + ketene products in the OH + allene reaction. We use the crossed laser-molecular beam apparatus to measure the distribution of velocities imparted to the Cl atoms upon photodissociation. The momentum-matched $CH_3C(O)CH_2$ radicals are formed under collision-free conditions, which facilitates characterization of their internal energy distribution and subsequent dynamics. We can detect the nascent radicals formed with a low enough internal energy to be stable to dissociation, as well as the dissociation products of the higher internal energy radicals.

Beyond the data presented herein, we also looked for signal at $m/e = 92$ ($CH_3C(O)CH_2Cl^+$), $m/e = 77$ ($COCH_2Cl^+$), $m/e = 57$ ($CH_3C(O)CH_2{}^+$), $m/e = 56$ ($C_3H_4O^+$), $m/e = 55$ ($C_3H_3O^+$), $m/e = 27$ ($C_2H_3{}^+$), and $m/e = 29$ ($C_2H_5{}^+$). For $m/e = 55$, 56, 57, and 77, little or no signal appeared above the noise after 1×10^6 laser shots. The signal acquired at $m/e = 92$ was used to verify the signal attributed to the photodissociation of molecular clusters in the beam. We observed about 30 000 counts in 6×10^6 laser shots, and the fit to this data is presented in the supplementary material.[7] The $m/e = 27$ and 29 data revealed both dissociative ionization of the neutral $m/e = 57$ parent, as well as neutral $m/e = 29$ signal resulting from a small channel out to C_2H_5 + CO; this channel proceeds via isomerization of the $CH_3C(O)CH_2$ radical to CH_3CH_2CO, which can then dissociate to CH_3CH_2 + CO.[8] These spectra are presented in a manuscript which is currently in preparation.[9]

B. Experimental method—Imaging apparatus

The velocity map imaging apparatus used in this work has been described previously;[10–14] only a brief description and modifications are provided here. We maintain a similar molecular beam seed ratio to the experiments taken in the scattering apparatus, using the equilibrium vapor pressure of chloroacetone at 25 °C seeded in He to a total stagnation pressure of 500 Torr. We expand the beam through a general valve Iota One pulsed valve, with an orifice diameter of 0.8 mm, and we heat the nozzle to 80 °C. After passing through a skimmer, the molecules are photodissociated with a vertically polarized 193.3 nm beam generated by a GAM (EX10F/300) ArF laser. We focus the beam such that the focal point lies roughly 1 cm beyond the intersection of the molecular beam and laser beams. We maintain pulse energies that are typically less than 1 mJ/pulse.

The photofragments are ionized by 118 nm light, fired ~40 ns after the photodissociation laser, which we generate by tripling the 355 nm output beam from a pulsed Nd:YAG laser (Continuum Surelite I-20).[14] Repeller and extractor plates, with a voltage ratio of 1.4:1, serve to accelerate the spherically expanding cloud of ions down a ~577 mm grounded time-of-flight tube toward the detector (Burle 3040FM). The detector consists of a position-sensitive chevron microchannel plate assembly (MCP) coupled to a P20 phosphor screen. We pulse the voltage on the front plate of the MCP to −750 V in order to coincide with the arrival time of ions having the desired mass-to-charge ratio. The phosphor screen is maintained at 3.3 kV above the potential of the rear MCP plate. A cooled charge-coupled device (CCD) camera (La Vision Imager 3), with a standard 35 mm lens, records the images. We process the obtained images using the ion-counting method, and the raw images are symmetrized about the vertical and horizontal axes in the data analysis.

We present images taken at $m/e = 42$ and $m/e = 15$, but not at other masses at which images were accrued, $m/e = 14$ (CH_2^+), $m/e = 29$ ($C_2H_5^+$), and $m/e = 27$ ($C_2H_3^+$). The $m/e = 14$ signal evidenced a speed distribution identical to that of the $m/e = 15$ (CH_3) signal, so we attribute it to multiphoton effects. This spectrum is shown in the supplemental material.[7]

In addition to these spectra taken with 10.5 eV photoionization, we also use 2+1 resonance-enhanced multiphoton ionization (REMPI) to detect the Cl photofragments that result from C–Cl bond fission. We use 235.33 nm ($4p^2D_{3/2} \leftarrow 3p^2P_{3/2}$) and 235.20 nm ($4p^2P_{1/2} \leftarrow 3p^2P_{1/2}$) to state-selectively ionize Cl($^2P_{3/2}$) and Cl($^2P_{1/2}$), respectively, as detailed in Ref 14. These images and associated spectra are given in the supplementary material.[7]

III. RESULTS AND ANALYSIS

The experimental data reveal two primary photodissociation channels of chloroacetone at 193 nm: C–Cl fission to produce Cl atoms and $CH_3C(O)CH_2$ radicals, along with C–C fission to form CH_2Cl and CH_3CO. No significant C–C bond fission to form CH_3 and $C(O)CH_2Cl$ is detected. We also investigate the dissociation of the radicals produced in the Cl bond fission channel, $CH_3C(O)CH_2$. Both the imaging and scattering data evidence branching to the CH_3 + ketene product channel. We analyze the results based on a part of the OH + allene potential energy surface presented in Sec. III B.

A. C–C bond fission of the $CH_3C(O)CH_2Cl$ precursor, yielding CH_3CO and CH_2Cl products

Figure 1 shows the time-of-flight spectrum taken at $m/e = 43$ (CH_3CO^+). The fastest portion of this signal is attributed to primary C–C bond fission in the precursor, $CH_3C(O)CH_2Cl$,

$$CH_3C(O)CH_2Cl + h\nu \rightarrow CH_3CO + CH_2Cl. \quad (1)$$

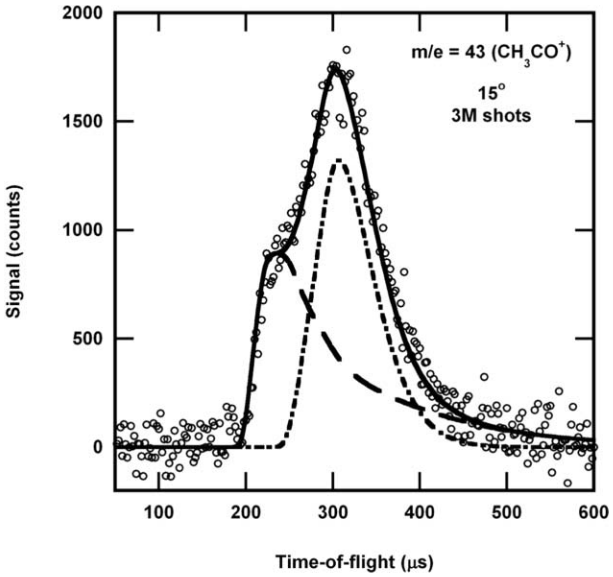

FIG. 1. Time-of-flight spectrum taken at $m/e = 43$ (CH_3CO^+) of the products resulting from the photodissociation of chloroacetone. The data are shown in open circles, and the total forward convolution fit to the data (shown in solid black line) is the sum of two contributions, shown here in long-dashed black and dash-dot-dashed black line. The long-dashed black line shows the contribution from the primary C–C fission of chloroacetone resulting in CH_3CO, detected at this mass-to-charge ratio, and its momentum-matched partner, CH_2Cl. Forward convolution fitting of this signal was used to derive the $P(E_T)$ shown in Fig. 2. The dash-dot-dashed line depicts the signal rising from molecular clusters in the beam.

Forward convolution fitting of the faster portion of this signal, shown in long-dashed black line, is used to derive the C–C bond fission recoil kinetic energy distribution, $P(E_T)$, shown in Fig. 2. Figure 3 displays the $m/e = 49$ (CH_2Cl^+) spectrum with its momentum-matched fit, as derived from the $P(E_T)$ shown in Fig. 2. The $m/e = 42$ spectrum, presented in Sec. III D, also has significant contributions from this C–C

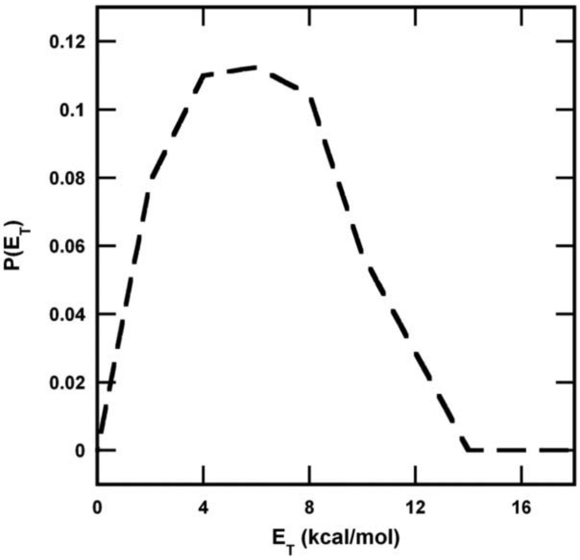

FIG. 2. The total recoil kinetic energy distribution, $P(E_T)$, of the CH_3CO and CH_2Cl fragments resulting from C–C bond fission in the photodissociation of chloroacetone. This fit was derived by forward convolution fitting of the fastest portion of the $m/e = 43$ (CH_3CO^+) signal in Fig. 1. This distribution was then used to predict the arrival time of the momentum-matched CH_2Cl partner photofragments, as seen in Fig. 3.

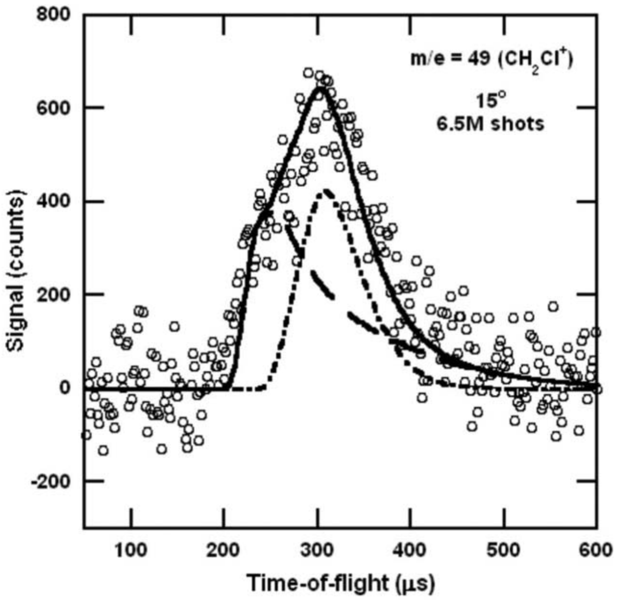

FIG. 3. Time-of-flight spectrum taken at *m/e* = 49 (CH_2Cl^+) of the signal resulting from the photodissociation of chloroacetone. The data are shown in open circles, and the total forward convolution fit to the data (shown in solid black line) is the sum of two contributions, shown here in long-dashed black and dash-dot-dashed black lines. The long-dashed black line shows the contribution from the primary C–C fission of chloroacetone resulting in CH_2Cl. This fit is derived from the $P(E_T)$ shown in Fig. 2. The signal shown in dash-dot-dashed lines is from molecular clusters in the beam.

bond fission channel; this will be discussed again in more detail in that section.

In both the *m/e* = 43 (CH_3CO^+) and *m/e* = 49 (CH_2Cl^+) spectra, there is a significant amount of signal that is not fit by the $P(E_T)$ from Fig. 2. This remaining signal, peaking near 300 μs, is attributed to the dissociation of molecular clusters [$(CH_3C(O)CH_2Cl)_n$] in the beam; as the cluster dissociates, a small recoil velocity may be imparted to the monomer. This signal, after accounting for small differences in ion flight times, appears in the *m/e* = 15 ($CH_3{}^+$), *m/e* = 35 (Cl^+), *m/e* = 42 ($COCH_2{}^+$), *m/e* = 43 (CH_3CO^+), *m/e* = 49 (CH_2Cl^+), and *m/e* = 92 ($CH_3C(O)CH_2Cl^+$) data. This component is derived from forward convolution fitting of the corresponding signal in the $CH_3{}^+$ spectrum, where it is easiest to distinguish and separate from other contributors. Because all spectra were taken under similar beam conditions, the resulting velocity distribution of this signal is used to fit the cluster contribution in all spectra in this paper. It is shown in dash-dot-dashed black line in all relevant figures.

B. C–Cl bond fission and the internal energy distribution of the nascent $CH_3C(O)CH_2$ radicals

Figure 4 shows the time-of-flight spectra taken at *m/e* = 35 (Cl^+); the upper, middle, and lower frames were taken with a source angle of 15°, 30°, and 45°, respectively. Most of this signal results from a primary C–Cl photofission process in the precursor, $CH_3C(O)CH_2Cl$,

$$CH_3C(O)CH_2Cl + h\nu \rightarrow Cl + CH_3C(O)CH_2. \qquad (2)$$

We used forward convolution fitting to derive the C–Cl bond fission recoil kinetic energy distribution, $P(E_T)$, shown

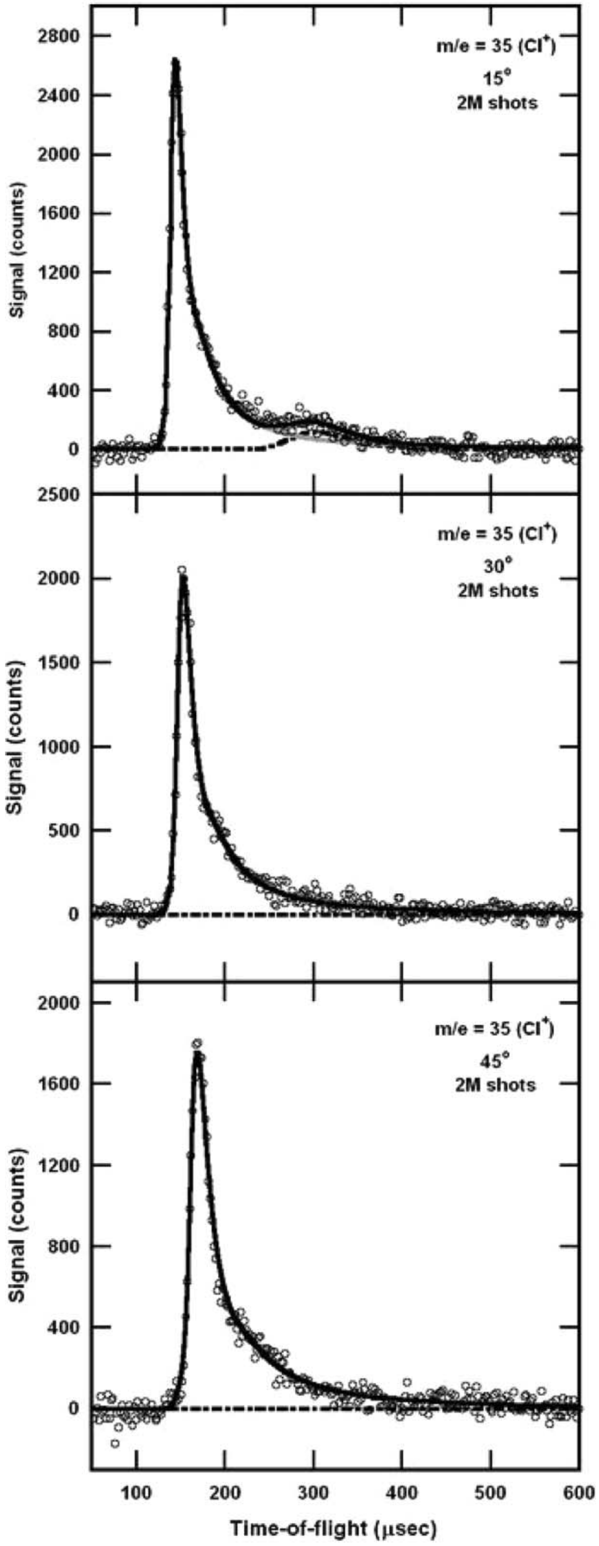

FIG. 4. Time-of-flight spectra corresponding to *m/e* = 35 (Cl^+) products resulting from the photodissociation of chloroacetone. The three frames displayed here are from data acquisition at 15°, 30°, and 45° (from top to bottom frame, respectively). The data are shown in open circles, and the total forward convolution fits to the data are shown in solid black line. The signal from Cl atoms produced in the C–Cl bond fission of chloroacetone at 193 nm to yield Cl atoms and $CH_3C(O)CH_2$ radicals is shown in solid gray line. This fit is used to derive the total recoil kinetic energy distribution shown in Fig. 5. The top frame, taken with a source angle of 15°, also shows a contribution from the photodissociation of molecular clusters in the beam; this contribution is shown in dash-dot-dashed black line.

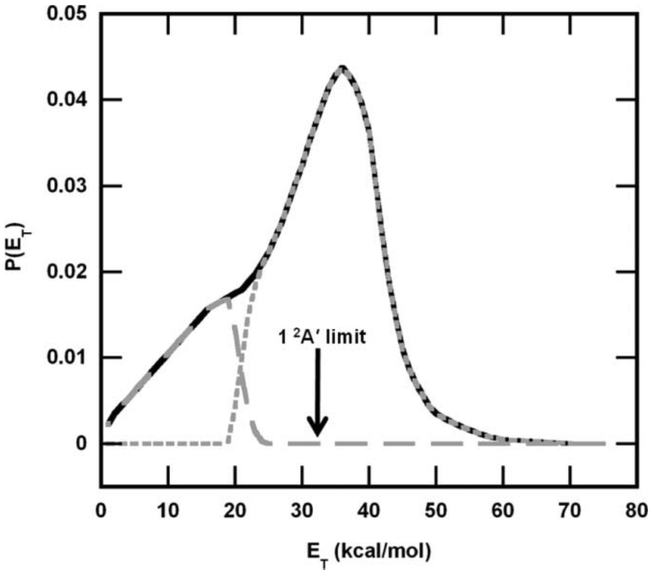

FIG. 5. The total recoil kinetic energy distribution, $P(E_T)$, derived from forward convolution fitting of the data taken at *m/e* = 35 (Cl^+), as shown in Fig. 4. The portion shown in dotted gray line has vibrational energies [based on Eq. (4)] below the barrier to dissociation to CH_3 + ketene—and thus the radicals formed with these kinetic energies are expected to be stable to dissociation. Likewise, those radicals formed with the range of recoil kinetic energies shown in long-dashed gray line have enough vibrational energy to dissociate. This distribution does not exhibit an abrupt cutoff $E_T = 21.9$ kcal/mol, as is calculated from Eq. (4), because here we include a thermal distribution of vibrational energies for $E_{\mathrm{chloroacetone}}$, rather than just the average of the distribution. The arrow marks the expected energetic limit for radicals in the excited $1^2A'$ state based on the calculated (Ref. 15) adiabatic excitation energy of 22 kcal/mol assuming the rotational energy partitioning is impulsive.

in the solid black line in Fig. 5. The shoulder that is present at lower kinetic energies is likely indicative of the formation of the nascent radicals in their low-lying $^2A'$ electronically excited state. Imaging experiments were also performed at *m/e* = 35; these images, along with the $P(E_T)$ obtained from them, are shown in the supplementary document and are in good qualitative agreement with our scattering results.[7] Lau calculated, using coupled cluster theory, CCSD(T), the adiabatic excitation energy of the first excited state to be about 22 kcal/mol.[15] The excited state radicals formed during the C–Cl bond fission could be formed with up to 32 kcal/mol partitioned in relative kinetic energy, if the rotational energy partitioning is impulsive as discussed below. This energetic limit is given by an arrow in Fig. 5. The analyses presented in this paper assume that any radicals that are formed in the $^2A'$ excited state dissociate via internal conversion to the ground state.

For those C–Cl bond fission events partitioning the highest relative kinetic energy to the recoiling Cl atoms, the momentum-matched $CH_3C(O)CH_2$ radicals are formed with low internal energies, some below the predicted dissociation barrier to CH_3 + ketene ($COCH_2$). The stable $CH_3C(O)CH_2$ radicals did not give signal at parent ion upon electron bombardment ionization, but instead gave signal at both *m/e* = 42 ($COCH_2^+$) and *m/e* = 15 (CH_3^+) daughter ions; these contributions will be detailed in Secs. III D and III E. The internal energy distribution of all nascent radicals, both stable and unstable, is determined from energy conservation, using the total recoil kinetic energy distribution shown in Fig. 5; this distribution is derived from the measured Cl atom velocities and momentum conservation. For each measured recoil kinetic energy, E_T, we calculate the internal energy in the nascent $CH_3C(O)CH_2$ radicals from

$$E_{\mathrm{int}}(CH_3C(O)CH_2) = h\nu + E_{\mathrm{chloroacetone}} - D_0(\mathrm{C{-}Cl}) - E_{\mathrm{Cl}} - E_T. \quad (3)$$

Here, the G3//B3LYP/aug-cc-pVTZ value of 73.7 kcal/mol is the dissociation energy of the C–Cl bond, D_0. The photon energy, $h\nu$, is 147.8 kcal/mol, and the energy in spin-orbit excitation of the Cl atom product is denoted E_{Cl}. $E_{\mathrm{chloroacetone}}$ is the internal energy of the precursor; it can be estimated by assuming that the rotational energy of the $CH_3C(O)CH_2Cl$ molecules is effectively cooled in the supersonic expansion, but the vibrational energy is characterized by a thermal distribution, with an average of 4.8 kcal/mol, at the nozzle temperature. E_{Cl} is 0 kcal/mol for $CH_3C(O)CH_2$ radicals produced in conjunction with ground state $Cl(^2P_{3/2})$ atoms and 2.5 kcal/mol for radicals produced in conjunction with spin-orbit excited state $Cl(^2P_{1/2})$ atoms. As this small additional internal energy is within the resolution of our experiments, it will be included with that of the radicals for plots in this paper.

The E_{int} term in the equation above is comprised of rotational, vibrational, and electronic energy of the nascent $CH_3C(O)CH_2$ radical formed in the dissociation. The high recoil kinetic energy products resulting from this C–Cl bond fission process partition a significant amount rotational energy to the departing $CH_3C(O)CH_2$ radical. Using the impulsive model described in Ratliff *et al.*,[16] and assuming that the impulsive force acts along the C–Cl bond at the geometry of the transition state on the S_1 excited state calculated by Liu and Fang,[17] we calculate an impact parameter, b, of 1.409 Å, and a moment of inertia for the nascent rotating radical, I, of 53.685 amu · Å^2. This geometry is given in the supplementary material.[7] Using the geometry at the C–Cl bond fission transition state in the impulsive model is more suitable because the excited state is not repulsive in the Franck–Condon region. Indeed, if one fits the data assuming impulsive forces at the ground state equilibrium geometry, the fit is noticeably worse; this fit is given in the supplementary documents for comparision.[7] Figure 6 shows the results of the calculations done by Fang *et al.* on the S_0 and S_1 electronic surfaces of chloroacetone. Their work reveals an excited electronic state of chloroacetone, the S_1 state, that lies 97.1 kcal/mol above the ground electronic state, the S_0 state. There is a 4.4 kcal/mol barrier (relative to the minimum of the S_1 state) as the C–Cl bond stretches out to $CH_3C(O)CH_2$ + Cl. This S_1 state is easily accessible upon excitation at 193 nm (147.8 kcal/mol), most likely via internal conversion from the S_2 state. We use the geometry of the transition state on the S_1 excited state to predict the portion of the $CH_3C(O)CH_2$ radicals, formed in the photodissociation of chloroacetone, that are stable to subsequent dissociation to CH_3 + ketene; this will be described in detail in Sec. III D. The rotational energy in the nascent radical, for each of the recoil kinetic en-

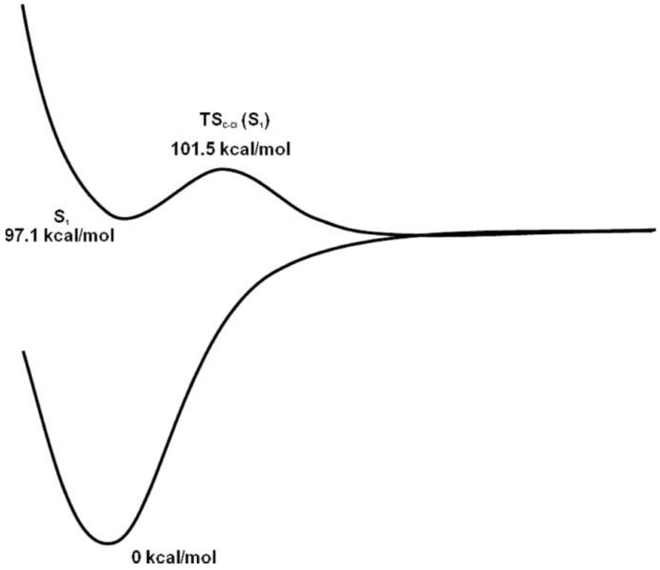

FIG. 6. Critical points on the S_0 and S_1 electronic surfaces of chloroacetone as calculated by Liu and Fang (Ref. 17) at the CAS (10,8)/cc-pVDZ level of theory. None of the energies include zero-point corrections. Their work reveals an excited electronic state of chloroacetone, the S_1 state, that lies 97.1 kcal/mol above the ground electronic state, the S_0 state. There is then a 4.4 kcal/mol barrier, relative to the minimum of the S_1 state, as the C–Cl bond stretches out to $CH_3C(O)CH_2$ + Cl. This S_1 state is easily accessible with the 147.8 kcal/mol photon imparted to the system, most likely via internal conversion from the S_2 state. We use the geometry of the transition state on the S_1 excited state, labeled here as $TS_{C\text{–}Cl}$ (S_1), in our impulsive model to predict the partitioning of rotational energy to the $CH_3C(O)CH_2$ radicals. This allows us to estimate the velocity spectra of the $CH_3C(O)CH_2$ radicals that are stable to subsequent dissociation to CH_3 + ketene.

ergies E_T, for C–Cl bond fission measured in the experiment, is given by $E_{\text{rot}} = \frac{\mu b^2}{I} E_T = 0.801 E_T$, where μ is the reduced mass of the dissociating fragments.

We can then substitute $E_{\text{vib}} + E_{\text{rot}}$ for the E_{int} term in Eq. (3) and solve for E_{vib}

$$\begin{aligned} &E_{\text{vib}}(CH_3C(O)CH_2) \\ &\quad = h\nu + E_{\text{chloroacetone}} - D_0(C{-}Cl) \\ &\qquad - E_{Cl} - (1 + 0.801)E_T. \end{aligned} \tag{4}$$

The top frame of Fig. 7 shows the derived internal energy distribution—both vibrational and rotational—of all of the $CH_3C(O)CH_2$ radicals superimposed on the relevant portion of the potential energy surface, as calculated at the G3//B3LYP/aug-cc-pVTZ level of theory[18] using the GAUSSIAN03 electronic structure package.[19] The zero-point-corrected energies are presented relative to the $CH_3C(O)CH_2$ radical; they are within 1.5 kcal/mol of the energies calculated at the CCSD(T) level of theory.[20] All of the relevant structures, moments of inertia, and harmonic vibrational frequencies are given in the supplementary material.[7] The fact that some of the radicals formed with internal energies above the dissociation barrier are stable is, again, due to the fact that some of that internal energy is partitioned into rotational energy.

The lower frame of Fig. 7 depicts the result of subtracting the energy in rotation at each E_T, therefore plotting only the vibrational energy distribution $P(E_{\text{vib}})$. We predict that any radicals formed with internal energies spanning the shaded region of the $P(E_{\text{int}})$ or $P(E_{\text{vib}})$ shown in Fig. 7 to be stable to secondary dissociation to CH_3 + $COCH_2$.

C. Detecting the stable $CH_3C(O)CH_2$ radicals

Only the $CH_3C(O)CH_2$ radicals that are momentum matched to the highest velocity Cl atoms are formed with low enough internal energies to lie below the dissociation barrier depicted in Fig. 7. Thus, using the predicted dissociation barrier of 39.5 kcal/mol, along with our model for predicting the amount of internal energy partitioned to rotation, we can use the fastest Cl atom velocities to predict the velocity spectrum and TOF spectrum of the stable $CH_3C(O)CH_2$ radicals. In the scattering lab, we saw no signal at $m/e = 57$ ($CH_3C(O)CH_2^+$) or at $m/e = 56$ or $m/e = 55$; accounting for flight time through the ionizer; however, we did see dissociative ionization of these radicals to $m/e = 42$ ($COCH_2^+$) and 15 (CH_3^+); these contributions are shown in Sec. III D and Sec. III E. We also note that no stable nascent radicals (at the parent ion of $m/e = 57$) were observed in the imaging experiments either, though this is likely due to dissociation of $CH_3C(O)CH_2^+$ to $C_2H_5^+$ + CO. Theoretical calculations on the cationic surface, along with images acquired at $m/e = 29$ ($C_2H_5^+$) offer experimental validation; a manuscript detailing these experiments is in preparation.[9]

D. Ketene + CH_3 from the dissociation of vibrationally excited $CH_3C(O)CH_2$ radicals

The $CH_3C(O)CH_2$ radicals that are formed in conjunction with the slowest Cl atoms are formed with enough vibrational energy to surmount the dissociation barrier to CH_3 + ketene products. A fit of the signal observed at $m/e = 42$ ($COCH_2^+$) is shown in Fig. 8. The contributions to that spectrum include dissociative ionization of the mass 57 ($CH_3C(O)CH_2$) neutral photofragments to $m/e = 42$ ($COCH_2^+$), $COCH_2$ (ketene) products formed from secondary dissociation of those $CH_3C(O)CH_2$ radicals formed with enough internal energy to surmount the barrier to CH_3 + ketene, dissociative ionization of the mass 43 (CH_3CO) neutral photofragment formed in the C–C bond fission channel described in Sec. III B and clusters. To definitively identify the signal from the dissociation of the $CH_3C(O)CH_2$ radical to CH_3 + ketene, we took imaging data at $m/e = 42$. The only source of $m/e = 42$ signal in the imaging lab is from ketene produced in the dissociation of highly vibrationally excited radicals. The $m/e = 42$ data, taken with a polarized 193 nm laser, exhibited a mildly velocity-dependent anisotropy; the signal exhibited a parallel distribution at the slower velocities, with a more perpendicular distribution at the faster velocities; a representative image can be seen in Fig. 9. Figure 10 shows plots of $P(v_{\text{ketene}})$ and $\beta(v_{\text{ketene}})$, in the upper and lower frames, respectively, spanning the relevant range of speeds. The $\beta(v_{\text{ketene}})$ distribution was well fit by a linear curve, allowing for a calculation of β at each v_{ketene} value. To accurately translate this information into a predicted time-of-flight distribution in the scattering lab, seen

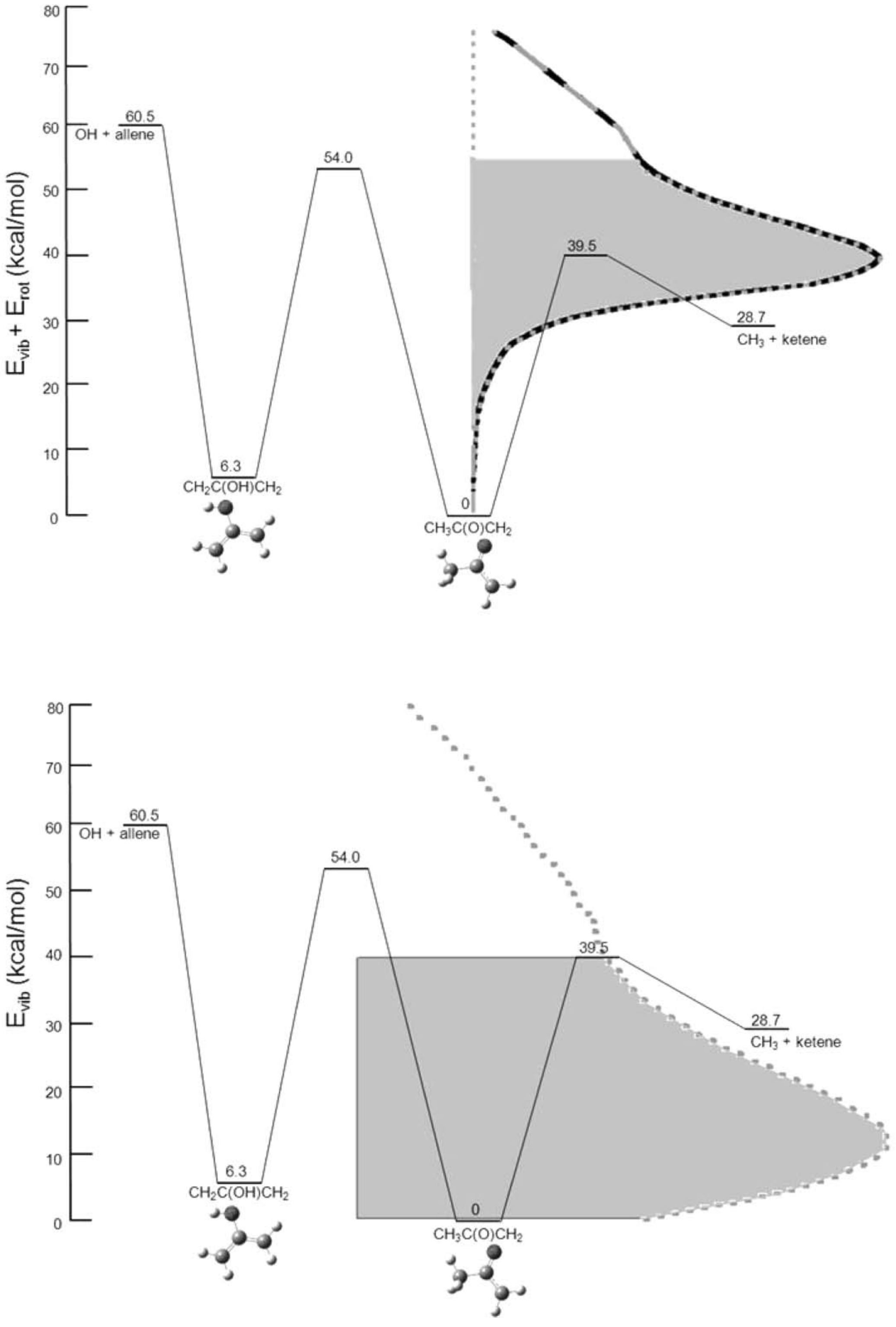

FIG. 7. The internal energy distribution of the nascent $CH_3C(O)CH_2$ radicals formed from C–Cl bond fission in the photodissociation of chloroacetone. The upper frame shows the internal energy distribution of the $CH_3C(O)CH_2$ radicals, as derived from the measured total recoil kinetic energy distribution in Fig. 5 and using the conservation of energy as given by Eq. (3). The lower frame explicitly shows the vibrational energy distribution of the nascent $CH_3C(O)CH_2$ radicals. Both of the distributions are superimposed on the zero-point corrected energies for the relevant minima and transition states of the OH + allene potential energy surface, where the OH adds to the center C atom of allene. All points are calculated at the G3//B3LYP level of theory. The structures were optimized at the B3LYP level of theory, using an aug-cc-pVTZ basis set, and they were converged to a root-mean-square (rms) force below 1×10^{-5} and a rms displacement below 4×10^{-5}, both in atomic units. The zero-point corrected energies are presented relative to the $CH_3C(O)CH_2$ radical. The radicals formed with lower internal energies, shown here in shaded gray, are predicted to be stable to dissociation to CH_3 + ketene. The fact that, in the upper frame, some have internal energies above the barrier to dissociation, but are stable, is again due to the fact that some energy has been partitioned to rotations. For the bottom frame, the rotational energy has been subtracted, and we present the pure $P(E_{\mathrm{vib}})$ distribution as calculated from Eq. (4). The higher recoil kinetic energy C–Cl bond fission events, producing radicals with a total internal energy below 30 kcal/mol, cannot dissociate from the assumed geometry, so we simply truncate the prediction in the lower frame of Fig. 7. We of course retain these radicals among the ones predicted to be stable to subsequent dissociation.

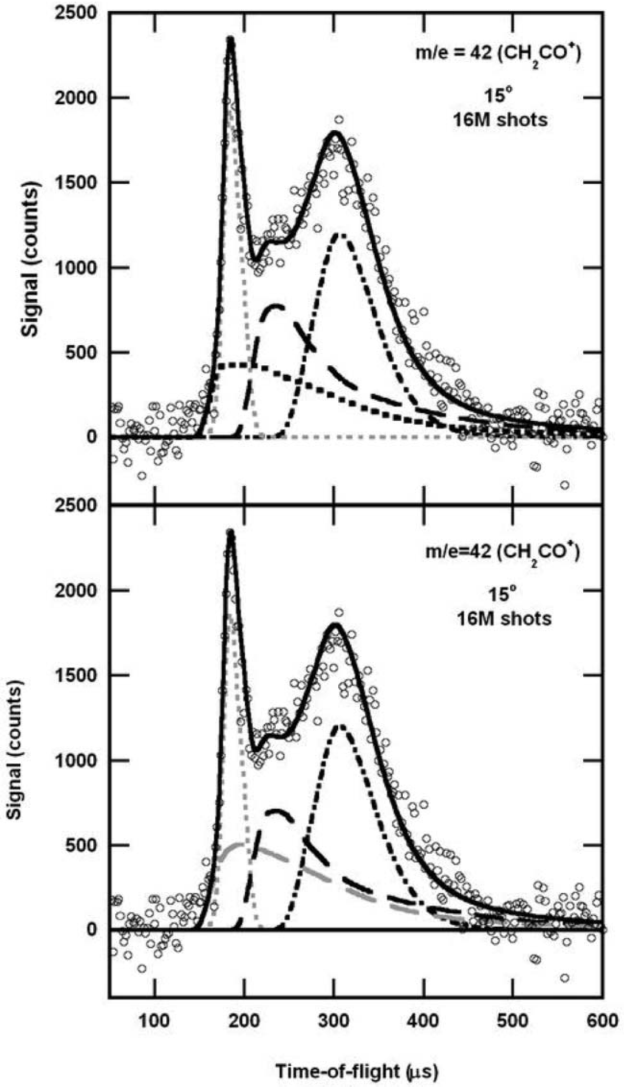

FIG. 8. Time-of-flight spectra of the signal at *m/e* = 42 ($COCH_2{}^+$) resulting from the photodissociation of chloroacetone and the subsequent dissociation of $CH_3C(O)CH_2$ radicals. The data are shown in open circles, and both the top and bottom frames have the overall fit shown in solid black line. The signal from ketene is shown by the broad component extending from 160 to 500 μs. These spectra also contain the contribution from neutral CH_3CO photoproducts dissociatively ionizing to *m/e* = 42, as well as the stable mass 57 $CH_3C(O)CH_2$ radicals dissociatively ionizing to *m/e* = 42, both upon 200 eV electron bombardment ionization; these fits are shown in long-dashed black line and dotted gray line, respectively. The top frame shows, in black dotted line, the signal assigned to ketene based on the $P(v_{\text{ketene}})$and $\beta(v_{\text{ketene}})$ from the imaging lab. The fits account for the fact that we are more sensitive to products with a parallel angular distribution, as they preferentially scatter in the detection plane. That same component is fit in the lower frame by considering the primary and secondary recoil velocities explicitly (see text for detail). A comparison between the fits to this broad component for ketene is given in the upper frame of Fig. 11.

in Fig. 11, we then scaled the individual points in the $P(v_{\text{ketene}})$ by $(1 + \beta/4)$; this is done to account for the fact that, even with an unpolarized laser, those photofragments with a parallel angular distribution are more likely to be scattered in the detector plane.[21] The remaining signal from monomer dissociation, that not fit by the dissociative ionization of the stable mass 57 radicals to *m/e* = 42 or by dissociative ionization of mass 43 to *m/e* = 42, is well fit by this scaled speed distribution; this fit is shown in dotted black line in the upper frame of Fig. 8.

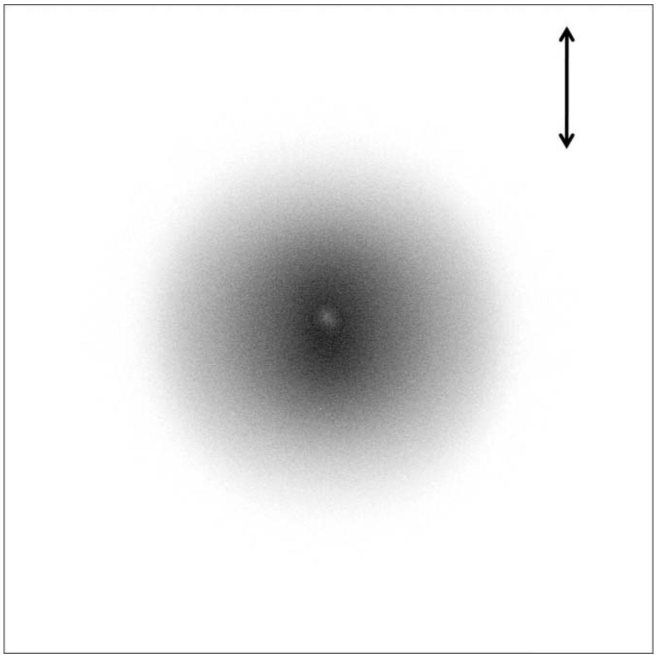

FIG. 9. Raw image of the *m/e* = 42 ($COCH_2{}^+$) products. It was obtained with 118 nm photoionization following photodissociation of chloroacetone at 193 nm. The photodissociation laser was polarized in the vertical plane of the image, as shown with the arrow. The image is 901 × 901 pixels and is the result of subtracting the background images obtained with 193 nm only and 118 nm only from the raw data.

The imaging data reveal only the *net* velocity imparted to the ketene products, the vector sum of the velocity imparted to the $CH_3C(O)CH_2$ radical in the initial C–Cl bond photofission with the velocity imparted when the nascent radical dissociates to CH_3 + ketene. Therefore, the plot of $P(v_{\text{ketene}})$ versus v_{ketene}, displayed in Fig. 10, shows on the *x*-axis the total magnitude of a vector that is the sum of two parts: $\vec{v}_{CH_3C(O)CH_2,1^\circ C-Cl} + \vec{v}_{COCH_2,2^\circ}$ Because the data are representative of the net ketene velocities, we must separately model the velocity imparted in the primary C–Cl bond fission, $\vec{v}_{CH_3C(O)CH_2,1^\circ C-Cl}$, and the additional velocity imparted as the radical dissociates to CH_3 + ketene, $\vec{v}_{COCH_2,2^\circ}$, in order to predict the net velocities of the momentum-matched CH_3 products. This also allows us to derive the distribution of energies imparted to relative translational energy when the $CH_3C(O)CH_2$ radicals dissociate to CH_3 + ketene. To do this, we first use the *m/e* = 42 imaging data to calculate where the *m/e* = 42 signal, detected in the imaging experiments, would show up in the scattering data. We use the $P(v_{\text{ketene}})$ and $\beta(v_{\text{ketene}})$ from the imaging experiments; this is the same predicted time-of-flight distribution shown in dotted black line in the top frame of Fig. 8. To fit this signal, we then consider both the velocities of the higher internal energy $CH_3C(O)CH_2$ radicals—those that have enough energy to dissociate to CH_3 and ketene—along with the range of kinetic energies imparted to the ketene and CH_3 fragments in the dissociation of these $CH_3C(O)CH_2$ radical. We can then iteratively manipulate the range of kinetic energies imparted in the secondary C–C bond fission, termed the secondary $P(E_T)$, until we get

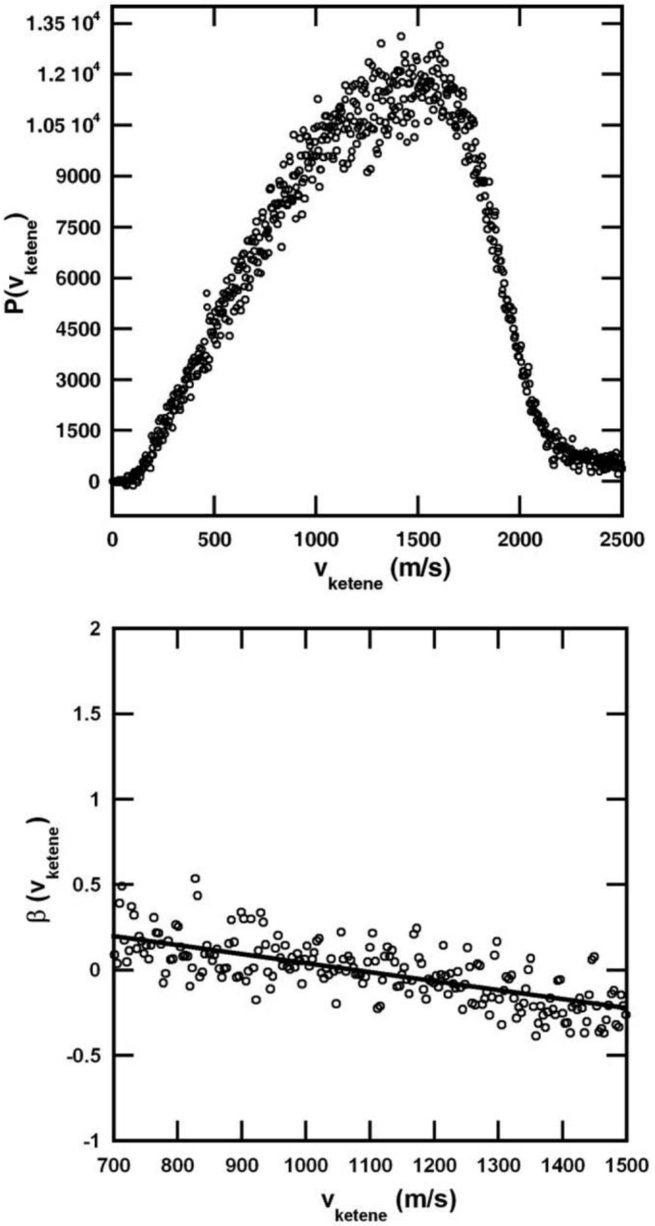

FIG. 10. Velocity distribution of the ketene products from the imaging data. The top frame shows the background-subtracted velocity distribution of the products detected at *m/e* = 42 ($COCH_2^+$). This velocity distribution is derived from the image shown in Fig. 9, which contains velocity-dependent anisotropies. In the scattering lab, the data are more sensitive to products with a parallel anisotropy, so we scale the individual points by $(1 + \beta/4)$ to generate the corresponding fits shown in the top frame of Fig. 8 and the top frame of Fig. 11. To derive the velocity-dependent anisotropy for this correction, we fit the $\beta(v_{\mathrm{ketene}})$ measured in the imaging apparatus to a line (shown in the bottom frame).

a predicted time-of-flight distribution that matches the actual observed signal. To calculate the velocities of the dissociating $CH_3C(O)CH_2$ radicals, we use the portion of the measured C–Cl bond fission $P(E_T)$ shown in long-dashed gray line in Fig. 5 and discussed in Sec. III D; the velocities predicted by this primary $P(E_T)$ are added to those calculated from the secondary $P(E_T)$ (found from the forward convolution fitting of the signal described above), to calculate the fit shown in long-dashed gray line superimposed on the signal in the upper frame of Fig. 11 and the lower frame of Fig. 8. The secondary $P(E_T)$, for the dissociation of $CH_3C(O)CH_2$ to CH_3 + ketene, used to obtain this fit is shown in Fig. 12.

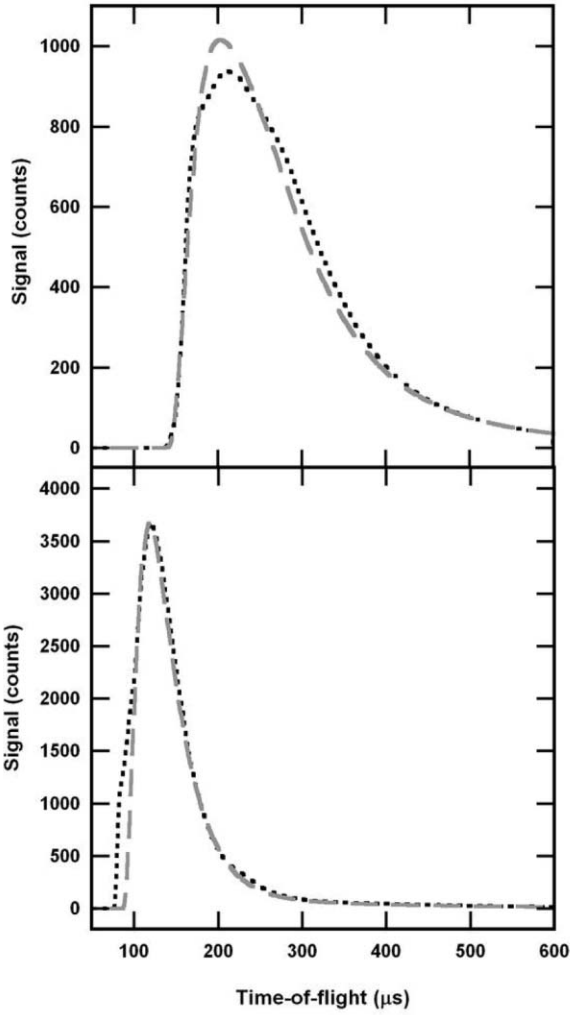

FIG. 11. Contributions of ketene to the *m/e* = 42 time-of-flight spectrum (upper frame) and the momentum-matched fit to the *m/e* = 15 (CH_3^+) observed signal (lower frame). In the upper frame, the dotted black line shows the portion of the time-of-flight at *m/e* = 42 attributed to ketene that is predicted by the imaging $P(v_{\mathrm{ketene}})$ and $\beta(v_{\mathrm{ketene}})$; this is the same fit that is shown in dotted black line in the upper frame of Fig. 8. The long-dashed gray line is the fit obtained by explicitly considering the velocities imparted in the primary photodissociation, along with those imparted as the higher internal energy radicals dissociate to CH_3 + ketene. The $P(E_T)$ that gives this fit, depicted in Fig. 12, is used to predict the time-of-flight in the scattering lab; this same fit is shown in the bottom frame of Fig. 8. Similarly, the lower frame shows the portion of the *m/e* = 15 time-of-flight that is predicted from the imaging $P(v_{\mathrm{methyl}})$ and $\beta(v_{\mathrm{methyl}})$; the long-dashed gray line is the momentum-matched fit based on the $P(E_T)$ used to fit the ketene signal. This is the same fit as shown in the bottom frame of Fig. 15.

We note that the velocity-dependent anisotropies seen in the imaging experiments for *m/e* = 42 were not accounted for in the fit shown in the bottom frame of Fig. 8, or in Fig. 11. While the anisotropy is noted, it is again a net anisotropy. We took imaging data at *m/e* = 35 to try and sort out the anisotropy resulting from primary C–Cl bond fission; the images reveal β values close to zero for the range of kinetic energies resulting in secondary dissociation to methyl and ketene. These $\beta(v_{\mathrm{Cl}})$ plots are given in the supplementary material.[7]

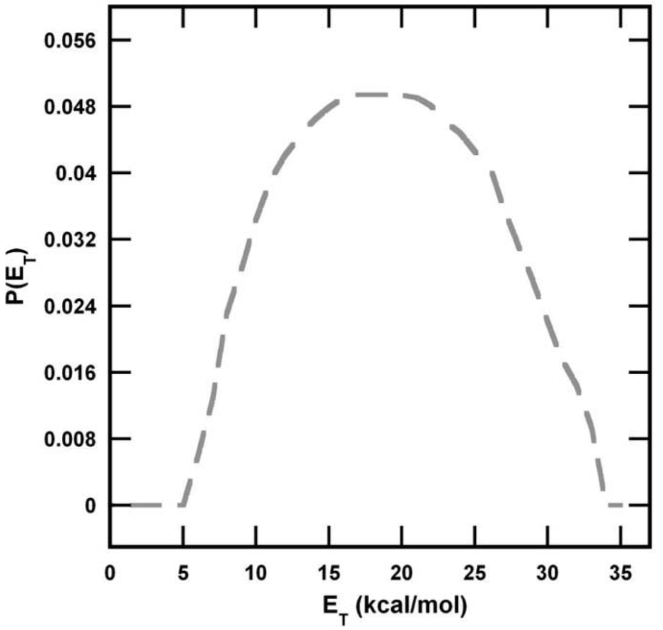

FIG. 12. The recoil translational energy distribution, $P(E_T)$, for the dissociation of vibrationally excited $CH_3C(O)CH_2$ radicals to CH_3 + ketene. Forward convolution fitting of the data shown in dotted black line in the upper frame of Fig. 11 was used to derive this $P(E_T)$. For the primary C–Cl bond fission, the low kinetic energy portion of the overall $P(E_T)$ shown in Fig. 5 was considered; this portion contains C–Cl fission recoil kinetic energies between 0 and 24 kcal/mol and is shown in long-dashed gray line in that figure. The $P(E_T)$ shown here is used to calculate the additional velocity imparted as the nascent $CH_3C(O)CH_2$ radicals dissociate to CH_3 + ketene. The resulting fits are shown in long-dashed gray line in Fig. 11.

To get the fit seen in Fig. 11, therefore, we simplify the procedure described in the preceding paragraph by assuming that both the primary and secondary distributions are isotropic. This is also supported, at least in part, by the small range of anisotropies shown in the bottom frame in Fig. 10. Were the range much bigger, e.g., spanning from 2 to −1, this approximation would not be as valid.

We also note that we used an isotropic angular distribution in the secondary fitting for the dissociation of the radical to CH_3 + ketene. The radicals are highly rotationally excited from the initial C–Cl bond photofission. Their rotational periods are typically much shorter than the dissociation lifetimes of the unstable radicals; an estimate for these timescales is given in the supplementary document.[7] Thus, the angular distribution of the recoil velocity vector of the CH_3 from the ketene must be symmetric about $\theta = 90^\circ$ (θ is the angle between the recoil velocity of the unstable radical and the secondary recoil velocity vectors of the CH_3 and ketene products from that radical). If the secondary dissociation were coplanar, the recoil velocity vectors of the CH_3 and ketene would be evenly distributed in the plane of rotation of the radical, reflecting the tangential recoil velocity of the two fragments, and one would expect a $\frac{1}{\sin(\theta)}$ angular distribution.[22] However the breaking C–C bond in the rotating radical is not in the plane of rotation; the axis of rotation is shown in the supplementary document.[7] Therefore. repulsive forces imparted as the C–C bond breaks would result in a substantial component perpendicular to the plane of rotation of the radical. This would smear the secondary angular distribution from the $\frac{1}{\sin(\theta)}$ distribution expected for coplanar scattering. An isotropic angular distribution fit the data quite adequately as shown in Fig. 11 and the lower frames of Figs. 8 and 15.

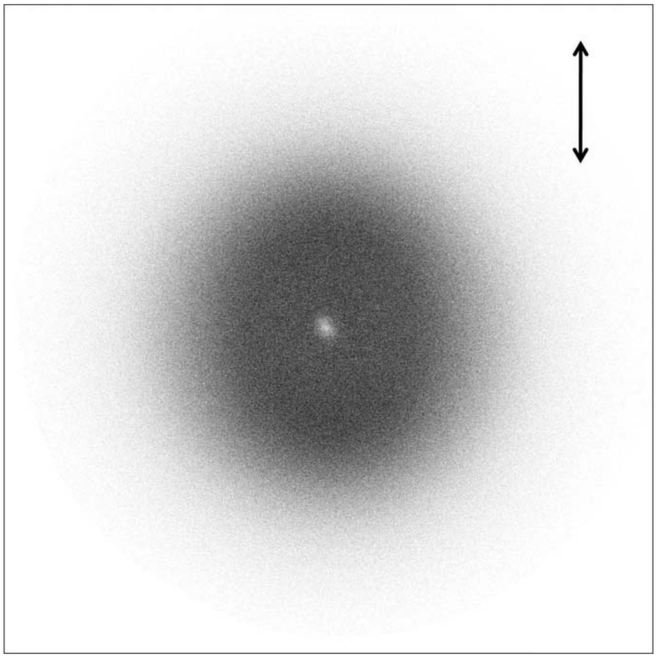

FIG. 13. Raw image of the *m/e* = 15 (CH_3^+) products. It was obtained with 118 nm photoionization following photodissociation of chloroacetone at 193 nm. The photodissociation laser was polarized in the vertical plane of the image, as shown with the arrow. The image is 901 × 901 pixels and is the result of subtracting the background images obtained with 193 nm only and 118 nm only from the raw data.

E. Momentum-matched methyl products from the dissociation of vibrationally excited $CH_3C(O)CH_2$ radicals to ketene + CH_3

The ketene products were formed in conjunction with CH_3. Signal at *m/e* = 15 (CH_3^+) was detected in both the imaging and the scattering lab. Figure 13 shows an image acquired at *m/e* = 15. In a manner similar to the analysis of the ketene spectrum, detailed in the above section, we plotted $P(v_{\text{methyl}})$ and $\beta(v_{\text{methyl}})$ from these experiments. These plots are shown in the upper and lower frames of Fig. 14, respectively. We then scale the individual points in the $P(v_{\text{methyl}})$ by $(1 + \beta/4)$. The upper frame of Fig. 15 shows this prediction, in dotted black line, superimposed on the actual observed signal, represented by the open circles. The bottom frame of Fig. 15 then shows the momentum-matched fit from secondary fitting of the *m/e* = 42 signal described in the previous section; this is the same fit shown in the bottom frame of Fig. 11. We note that this two-step process fits the CH_3 signal quite well, save the highest velocity CH_3 products arriving before 100 μs. While, in principle, the CH_3 products could result from either C–CH_3 photofission or from the dissociation of the $CH_3C(O)CH_2$ radicals formed in the primary C–Cl bond fission, the agreement between the distributions of velocities detected for the ketene products and the velocity detected for

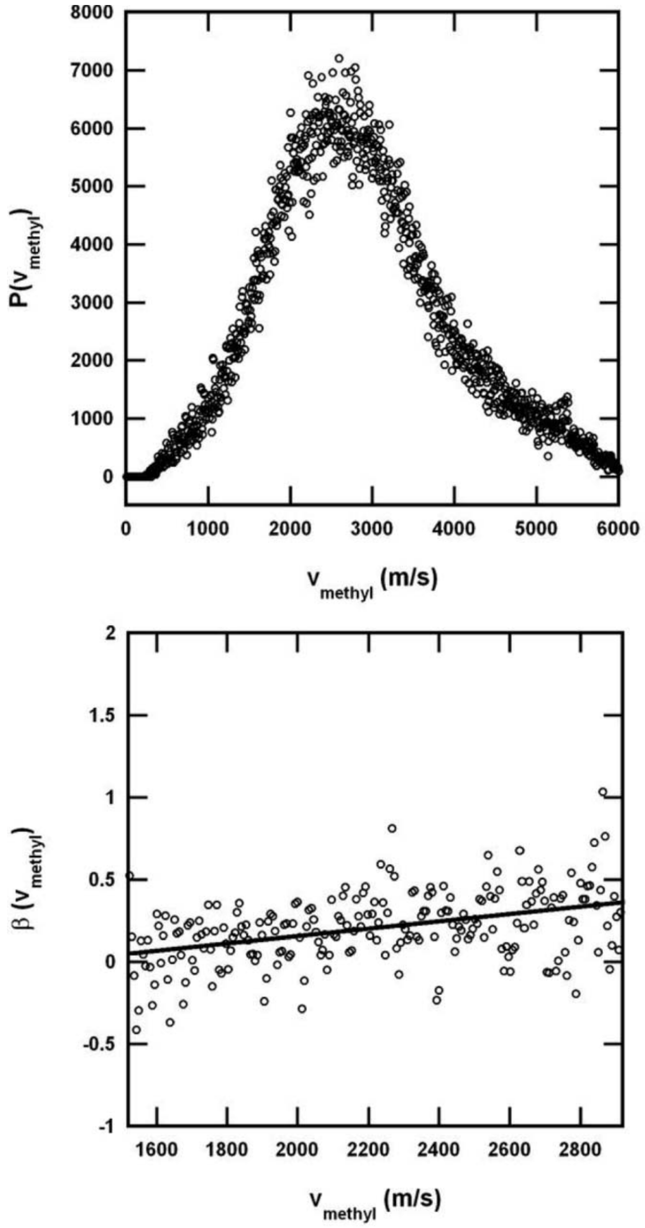

FIG. 14. Velocity distribution of the CH_3 products from the imaging data. The top frame shows the background-subtracted velocity distribution of the products detected at $m/e = 15$ (CH_3^+). This velocity distribution is derived from the image shown in Fig. 13, which contains velocity-dependent anisotropies. In the scattering lab, the data are more sensitive to products with a parallel anisotropy, so we scale the individual points by $(1 + \beta/4)$ to generate the corresponding contributions shown in the lower frame of Fig. 11 and in black dotted line in the top frame of Fig. 15. To derive the velocity-dependent anisotropy for this correction, we fit the $\beta(v_{\mathrm{methyl}})$ measured in the imaging apparatus to a line (shown in the bottom frame).

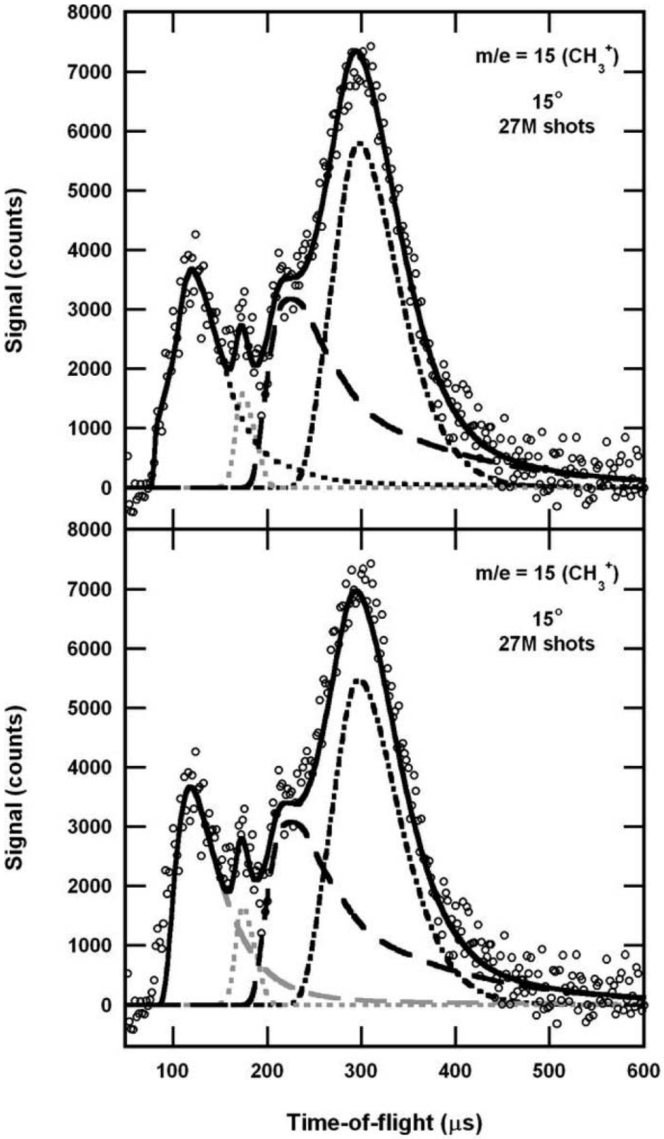

FIG. 15. Time-of-flight spectra taken at $m/e = 15$ (CH_3^+). The data are shown in open circles, and both the top and bottom frames have the overall fit shown in solid black line. These spectra also contain the contribution from neutral CH_3CO photofragments dissociatively ionizing to $m/e = 15$, as well as stable $CH_3C(O)CH_2$ radicals (mass 57) dissociatively ionizing to $m/e = 15$, both upon 200 eV electron bombardment ionization; these fits are shown in long-dashed black line and dotted gray line, respectively. The top frame has the contribution predicted based on the $P(v_{CH_3})$ from the imaging lab. The long-dashed gray line in the bottom frame is the predicted time-of-flight based on the fit from Fig. 11, where the primary (initial C–Cl bond photofission) and secondary (subsequent C–C bond fission in the nascent $CH_3C(O)CH_2$ radical) processes have been explicitly considered.

the CH_3 products shows that the dissociating radicals produce nearly all of our CH_3 signal.

F. Branching ratio for C–Cl bond fission and C–C bond fission

We used the signal acquired at $m/e = 42$ ($COCH_2^+$) and $m/e = 35$ (Cl^+) to estimate a rough branching ratio between the C–Cl bond photofission channel and the C–C bond photofission channel. To do this, we integrated the signal under the corresponding fits of the $m/e = 42$ and $m/e = 35$ spectra (channels 65–120 for the $m/e = 35$ spectrum and channels 100–150 for the $m/e = 42$ spectrum). We give the ratio of signals below as $\mathrm{obs}(^{35}Cl^+/CH_2CO^+)$. We then correct this signal for isotopic abundances of ^{35}Cl ($f_{^{35}Cl}$), expected signal based on kinematic corrections and Jacobian factors (including transit time through the ionizer), the electron bombardment ionization cross sections σ_{ion}, and the daughter ion fragmentation patterns, $(f_{CH_2CO^+/CH_3CO}/f_{Cl^+/Cl})$. We obtain

$$\begin{aligned}\frac{\sigma_{\mathrm{C-Cl}}}{\sigma_{\mathrm{C-C}}} &= \mathrm{obs}\left(\frac{{}^{35}\mathrm{Cl}^{+}}{\mathrm{CH_2CO^{+}}}\right)(f_{^{35}\mathrm{Cl}})^{-1}\left(\frac{\text{expected signal with } \mathrm{CH_2CO} \text{ kinematics}}{\text{expected signal with Cl kinematics}}\right)\left(\frac{\sigma_{\mathrm{ion,CH_3CO}}}{\sigma_{\mathrm{Cl}}}\right)\left(\frac{f_{\mathrm{CH_2CO^{+}/CH_3CO}}}{f_{\mathrm{Cl^{+}/Cl}}}\right)\\ &= \left(\frac{0.021181}{0.00195}\right)(0.7578)^{-1}\left(\frac{0.503}{0.128}\right)\left(\frac{72.5}{35.15}\right)\left(\frac{0.094}{1}\right) = 10.9. \qquad (5)\end{aligned}$$

The electron bombardment ionization cross sections are estimated roughly from the empirical formula proposed by Center and Mandl,[23] with the sum of atomic polarizabilities calculated from those of Miller and Bederson.[24] This estimate is not expected to be better than ±20%. We use the daughter ion cracking pattern of CH_3CO radicals (appearing as CH_3CO^+) presented in Kitchen *et al.*[4] They reported a value of 0.094 ± 0.002 for the daughter ion production probability, $f_{CH_2CO^+/CH_3CO}$, at 200 eV. The numbers presented in the equation above are from a representative set of $m/e = 42$ and $m/e = 35$ spectra. We repeated this process with ten different pairs of spectra, and the results were consistent, yielding values of 11 ± 0.6 for the $\sigma_{C-Cl}/\sigma_{C-C}$ branching ratio.

IV. DISCUSSION

The results presented in this paper evidence the wavelength-dependent primary photofission channels of chloroacetone in the ultraviolet. More importantly, however, the data reveal dissociation dynamics of a key radical intermediate of the reaction of OH with allene. We discuss the latter first, as it offers an additional channel that might contribute to the mechanism for the OH-initiated oxidation of volatile organic compounds currently included in atmospheric models—specifically when the VOC contains a C=C=C moiety.

At high collision energies, the reaction of OH with an alkene can proceed by either H atom abstraction, or via an addition mechanism. While the overall rates of such reactions are well characterized as a function of temperature and pressure, the product branching between these two channels is uncertain. At 300 K, the addition channel dominates because there are few high energy collisions. Atmospheric models assume that the addition complex, stabilized via inelastic collisions, does not unimolecularly dissociate, but rather that it survives to react with other atmospheric species such as O_2. Recent theoretical results of Senosiain *et al.*[25] confirm that, while the reaction of OH with ethene results in significant branching to CH_3 + formaldehyde under collision-free conditions at 300 K, it results in nearly exclusively stabilized C_2H_4OH adduct when collisions with an atmosphere of N_2 are included in the dynamics. In atmospheric models,[26,27] the subsequent reaction of the stabilized adduct with O_2 results in peroxy radicals that then react with other species in the atmosphere, such as NO and HO_2; these go on to form low volatility products that contribute to the formation of secondary organic aerosols.[28] We explain below why one might expect the reaction of OH with allene, or other species with a C=C=C moiety like 1,2-butadiene or 3-methyl-1,2-butadiene, to exhibit an additional product channel whereby the radical adduct isomerizes and unimolecularly dissociates to ketene + an alkyl radical. The collisional stabilization of the radical $CH_3C(OH)CH_2$ adduct then competes with this dissociation channel.

To understand why the oxidation of allene (or 1,2-butadiene, or 3-methyl-1,2-butatidiene) with OH at the center C atom might differ from other unsaturated volatile organic compounds, you need only examine the relative energies in Fig. 7. On average, the inelastic collisions with N_2 remove internal energy from the nascent $CH_2C(OH)CH_2$ adduct, thereby resulting in adducts unable to redissociate to OH + allene. Unlike the adduct formed from OH with many alkenes, the adduct of OH with allene can easily isomerize and dissociate directly to CH_3 + ketene. Although a few collisions with N_2 can remove a kcal/mol or two of energy and bring the internal energy of the $CH_2C(OH)CH_2$ radical adduct below the asymptotic energy to dissociate back to OH + allene, the adduct may still have enough energy to surmount the isomerization barrier to $CH_3C(O)CH_2$ and dissociate to CH_3 + ketene. The isomerization barrier lies below the energy required to redissociate to OH + allene (6.5 kcal/mol lower at the G3 level of theory and 7.9 kcal/mol lower at the CCSD(T) level). This is quite different than the OH adducts formed upon addition to species like ethene or propene, whose barriers for isomerization are higher than, not lower than, the asymptotic OH + alkene energy.

To assess the competition between collisional stabilization of the $CH_2C(OH)CH_2$ adduct and its isomerization and subsequent dissociation to CH_3 + ketene, we carried out a rough simulation using the MULTIWELL program suite.[29–32] The calculations suggest that the branching to the CH_3 + ketene channel is small, on the order of a few percent at most, even when 1D Eckart tunneling through the isomerization is included (see supplementary documents[7]). We expect an analogous reaction of OH with 1,2-butadiene and 3-methyl-1,2-butadiene, with the products of the addition of OH to the center atom in the C=C=C moiety being ketene plus an alkyl radical (ketene + ethyl in the case of the reaction of OH with 1,2-butadiene and ketene + 2-propyl in the reaction of OH with 3-methyl-1,2-butadiene.)

Thus, the kinetic mechanism currently assumed in atmospheric models for reaction of OH with volatile organic compounds with C=C=C moieties is largely valid (the current mechanism presented in SAPRC-07 for the reaction of OH with 1,2-butadiene is given in the supplementary document[7]). Although that mechanism omits the ketene + alkyl product channel that channel is likely to be minor at atmospheric pressures. Most of the OH + 1,2 dialkene adducts are collisionally stabilized.

The photochemistry of chloroacetone is also of current interest. Burkholder *et al.*[2] have examined the UV absorption cross sections from 200 to 360 nm for both chloroacetone and bromoacetone. They also measured product quantum yields for CO, CO_2, formic acid, and HCl in the bulk kinetic system at 308 and 351 nm. The primary photodissociation channels of chloroacetone could not be examined in those studies, as the primary products are radical species, but two prior experiments under collision-free conditions have studied the primary photofission channels. Waschewsky *et al.*[3] investigated the primary photofission channels of chloroacetone at 308 nm, finding that C–Cl bond fission dominated; they detected only a small contribution from C–C photofission to form CH_2Cl + CH_3CO. Kitchen and co-workers later determined the branching ratio between these two photofission channels at 308 nm to be C–Cl:C–C = 4.6:1.[4] The branching ratio that we calculated based on these experiments at 193 nm is a larger, 11:1, showing that the relative branching to the C–C fission channel decreases markedly for excitation at 193 nm. These photoreactions likely proceed via excitation to the S_2 excited state, followed by internal conversion to the S_1 state. Fang and co-workers have investigated the photofission channels of acetyl chloride on S_1; they find that the C–C fission channel has a higher energetic barrier than the C–Cl fission channel.[33] If the observed C–C fission channel in chloroacetone also has a higher barrier than C–Cl fission, and if the dynamics of chloroacetone photodissociation occur also on an S_1 excited state for both excitation at 308 and 193 nm (perhaps due to internal conversion from S_2 to S_1), then a statistical model would predict that the C–C fission channel would gain importance as the excitation energy increases, not decrease as observed here. Understanding the observed product branching awaits calculations of the nonadiabatic quantum dynamics on the S_1 and S_2 excited states.

Finally, the data presented here demonstrate that the energetically stable $CH_3C(O)CH_2$ radicals gave signal at the $m/e = 15$ and $m/e = 42$ daughter ions, but not at parent ion, $m/e = 57$, or the daughter ions $m/e = 56$ or 55 upon 200 eV electron bombardment ionization. Though extensive fragmentation of ions produced from electron bombardment is not unusual, even 10.5 eV photoionization did not give signal at the parent ion in our imaging experiments. To understand this, we undertook G3//B3LYP calculations on the critical points on the potential energy surface of the cation. Our calculations show that there is a low (<0.5 eV) isomerization barrier to $CH_3CH_2CO^+$ on the cationic surface, with subsequent dissociation to $C_2H_5{}^+$ + CO products. We took images at both $m/e = 29$ ($C_2H_5{}^+$) and $m/e = 27$ ($C_2H_3{}^+$) to gain further insight into the dissociative dynamics of this cationic species. A manuscript detailing these experiments is in preparation.[9]

ACKNOWLEDGMENTS

This work was supported by the National Science Foundation under Grant number CHE-0746050 (Butler). We gratefully acknowledge Professor K.-C. Lau for providing us with his CCSD(T) results on the $2A'$ excited state of the radical, as well as Professor Wei-Hai Fang and his student Li-Hong Liu for their CASSCF results on the equilibrium geometry and transition state for C–Cl fission on the S_1 excited state of chloroacetone. We also thank Professor W. P. L. Carter for useful discussions and C. C. Womack for her help taking the imaging data presented in the supplementary documents.

[1] A. S. Raman, M. J. Bell, K.-C. Lau, and L. J. Butler, J. Chem. Phys. **127**, 154316 (2007).
[2] J. B. Burkholder, M. K. Gilles, T. Gierczak, and A. R. Ravishankara, Geophys. Res. Lett. **29**, 1822 (2002).
[3] G. C. Waschewsky, P. W. Kash, T. L. Myers, D. C. Kitchen, and L. J. Butler, J. Chem. Soc., Faraday Trans. **90**, 1581 (1994).
[4] D. C. Kitchen, T. L. Myers, and L. J. Butler, J. Phys. Chem. **100**, 5200 (1996).
[5] Y. T. Lee, J. D. McDonald, P. R. LeBreton, and D. R. Herschbach, Rev. Sci. Instrum. **40**, 1402 (1969).
[6] N. R. Daly, Rev. Sci. Instrum. **31**, 264 (1960).
[7] See supplementary material at http://dx.doi.org/10.1063/1.3525465 for the G3//B3LYP/aug-cc-pVTZ energies at 0 K geometries, and the vibrational frequencies of the important minima and transition states on the OH + allene potential energy surface used to estimate the importance of the CH_3 + ketene product channels under conditions of an atmosphere of pressure of N_2 (and some additional details on that estimate). It also gives supplemental imaging and scattering data and details on how the rotational energy in the nascent radicals is estimated.
[8] B. L. FitzPatrick, "Theoretical study of isomerization and dissociation transition states of C_3H_5O radical isomers: *Ab initio* characterization of the critical points and statistical transition state theory modeling of the dynamics," J. Phys. Chem. A (submitted).
[9] B. W. Alligood, C. C. Womack, and L. J. Butler, "Dissociative photoionization of $CH_3C(O)CH_2$ to $C_2H_5{}^+$," Int. J. Mass. Spectrom. (submitted, 2011).
[10] A. J. R. Heck and D. W. Chandler, Annu. Rev. Phys. Chem. **46**, 335 (1995).
[11] A. T. J. B. Eppink and D. H. Parker, Rev. Sci. Instrum. **68**, 3477 (1997).
[12] Y. Sato, Y. Matsumi, M. Kawasaki, K. Tsukiyama, and R. Bersohn, J. Phys. Chem. **99**, 16307 (1995).
[13] Y. Liu, and L. J. Butler, J. Chem. Phys. **121**, 11016 (2004).
[14] B. J. Ratliff, X. N. Tang, L. J. Butler, D. E. Szpunar, and K.-C. Lau, J. Chem. Phys. **131**, 044304 (2009).
[15] K.-C. Lau (private communication, May 2010).
[16] B. J. Ratliff, C. C. Womack, X. N. Tang, W. M. Landau, L. J. Butler, and D. E. Szpunar, J. Phys. Chem. A **114**, 4934 (2010).
[17] L.-H. Liu and W.-H. Fang (private communication, April 2010).
[18] A. G. Baboul, L. A. Curtiss, P. C. Redfern, and K. Raghavachari, J. Chem. Phys. **110**, 7650 (1999).
[19] M. J. Frisch, G. W. Trucks, H. B. Schlegel *et al.*, *GAUSSIAN 03, Revision C.02*, Gaussian, Inc., Pittsburgh, PA, 2003.
[20] Benjamin FitzPatrick, Ph.D. thesis, University of Chicago, 2010.
[21] Laurie J. Butler, Ph.D. thesis, University of California, Berkeley, 1985.
[22] B. L. FitzPatrick, B. W. Alligood, L. J. Butler, S.-H. Lee, and J. J. Lin, J. Chem. Phys. **133**, 094306 (2010).
[23] R. E. Center and A. Mandl, J. Chem. Phys. **57**, 4104 (1972).
[24] T. M. Miller and B. Bederson, Adv. At. Mol. Phys. **13**, 1 (1977).
[25] J. P. Senosiain, S. J. Klippenstein, and J. A. Miller, J. Phys. Chem. A **110**, 6960 (2006).
[26] The Master Chemical Mechanism at http://mcm.leeds.ac.uk/MCM.
[27] W. P. L. Carter, Development of the SAPRC-07 Chemical Mechanism and Updated Ozone Reactivity Scales, Final Report to the California Air Resources Board, Contract No. 03-318, June 2009.
[28] J. H. Kroll and J. H. Seinfeld,Atmos. Environ. **42**, 3593 (2008).
[29] MULTIWELL-2010 Software, 2010, designed and maintained by John R. Barker with contributors Nicholas F. Ortiz, Jack M. Preses, Lawrence L. Lohr, Andrea Maranzana, Philip J. Stimac, T. Lam Nguyen, and T. J. Dhilip Kumar, University of Michigan, Ann Arbor, MI, http://aoss.engin.umich.edu/multiwell/.
[30] J. R. Barker, Int. J. Chem. Kinet. **33**, 232 (2001).
[31] J. R. Barker, Int. J. Chem. Kinet. **41**, 748 (2009).
[32] T. L. Nguyen and J. R. Barker, J. Phys. Chem. A **114**, 3718 (2010).
[33] S.-L. Chen and W.-H. Fang, J. Phys. Chem. A **111**, 9355 (2007).